



HAL
open science

Nonlinear properties and structural rearrangements in thermally poled niobium germanate glasses

Lia Mara Marcondes, Juliane Resges Orives, Frédéric Adamietz, Gael Yves Poirier, Thierry Cardinal, Marc Dussauze, Marcelo Nalin

► **To cite this version:**

Lia Mara Marcondes, Juliane Resges Orives, Frédéric Adamietz, Gael Yves Poirier, Thierry Cardinal, et al.. Nonlinear properties and structural rearrangements in thermally poled niobium germanate glasses. *Journal of Non-Crystalline Solids*, 2024, 627, pp.122809. 10.1016/j.jnoncrysol.2023.122809 . hal-04410194

HAL Id: hal-04410194

<https://hal.science/hal-04410194>

Submitted on 22 Jan 2024

HAL is a multi-disciplinary open access archive for the deposit and dissemination of scientific research documents, whether they are published or not. The documents may come from teaching and research institutions in France or abroad, or from public or private research centers.

L'archive ouverte pluridisciplinaire **HAL**, est destinée au dépôt et à la diffusion de documents scientifiques de niveau recherche, publiés ou non, émanant des établissements d'enseignement et de recherche français ou étrangers, des laboratoires publics ou privés.



Contents lists available at ScienceDirect

Journal of Non-Crystalline Solids

journal homepage: www.elsevier.com/locate/jnoncrsol

Nonlinear properties and structural rearrangements in thermally poled niobium germanate glasses

Lia Mara Marcondes^{a,*}, Juliane Resges Orives^a, Frederic Adamitez^d, Gael Yves Poirier^b,
Thierry Cardinal^c, Marc Dussauze^{d,*}, Marcelo Nalin^a

^a Institute of Chemistry, São Paulo State University - UNESP, Araraquara, SP, Brazil

^b Institute of Science and Technology, Federal University of Alfenas, Poços de Caldas-MG, Brazil

^c Institut de Chimie de la Matière Condensée de Bordeaux, Université de Bordeaux, 87 Avenue du Dr Schweitzer, F-33608, Pessac, France

^d Institut des Sciences Moléculaires, UMR 5255, Université de Bordeaux, 351 cours de la Libération, 33405 Talence Cedex, France

ARTICLE INFO

Keywords:

Glass
Thermal poling
Nonlinear optics

ABSTRACT

Second order nonlinear optical properties and structural rearrangements in $\text{GeO}_2\text{-Na}_2\text{O-Nb}_2\text{O}_5$ glasses were achieved by thermal poling. The effects of applied voltage as well as sodium and niobium contents on nonlinear optical (NLO)-active layer were investigated. Structural rearrangements in the anodic microlayer were investigated and occur due to sodium depletion promoting variation in bridging/non-bridging oxygen ratio and formation of a more polymerized network. Quantitative analysis of second harmonic generation signals confirm the electrooptical origin of the nonlinear optical response described by the electric-field-induced second harmonic model. $\chi^{(2)}$ susceptibility values range from 0.42 to 0.76 pm/V depending on the niobium content. Lastly, the charge compensation mechanism with increasing applied voltage was described in detail. A progressive decrease in $\chi^{(2)}$ for higher voltages was observed due to a greater poled thickness than expected by classical electrostatic models. In this case, the compensation mechanism occurs due to structural rearrangement, redox reactions, and motion of negative charges.

1. Introduction

Glassy materials as based materials for photonic devices have been increasingly highlighted due to the simple manufacture and the possibility of adjusting the composition, which consequently allows the adjustment of specific properties [1–3]. Glasses feature a high transmission window [4,5] and a wide variety of sizes and shapes such as cylindrical [6–8] and ribbon [9] fibers, bulk [10], powders [11] and thin films [12,13]. Furthermore, despite their isotropic nature, these materials may exhibit second order nonlinear optical susceptibility ($\chi^{(2)}$) by locally breaking the centrosymmetry using techniques such as thermal [14,15] and optical [16,17] poling. In this perspective, implemented nonlinear optical (NLO) properties and wide glass-based matrix transmission window have been promising for NLO photonic applications as wavelength conversion [18,19] and electro-optical devices [20].

Thermal poling process started in 1969 [21] and is a simple and low cost surface modification technique. By this technique, a non-crystalline material is heated, and a DC electric field is applied, resulting in

modification of the anodic surface of the material [22]. The NLO responses after thermal poling was only reported more than twenty years later [23] and occurs due to a break of centrosymmetry associated with the space charge formation and a resulting static electric field [22]. In more detail, an effective second order optical susceptibility is induced by an electrooptical effect, coming from the interaction of a permanent implemented static electric field (E_{stat}) and the third order non-linear susceptibility $\chi^{(3)}$, according to the relationship $\chi^{(2)} = 3\chi^{(3)}E_{\text{stat}}$ [24–26].

NLO properties in thermally poled glasses have been studied in various glass systems covering pure silica [23], silicate [24,25], phosphate [27], germanate [28], sulfide [29], for example. Niobium germanate glasses are considered promising due to their transparency in a large spectral range including the mid-IR [30] and NLO properties of glasses with highly polarizable NbO_6 polyhedra [31]. These matrices have a mixed $\text{GeO}_4\text{-NbO}_6$ network and the high Nb_2O_5 content allows the formation of NbO_6 clusters [32] enhancing NLO properties [31,33]. Regarding the high efficiency of NLO devices, other dielectric crystalline

* Corresponding authors at: Instituto de Química, Universidade Estadual Paulista Júlio de Mendonça Filho – UNESP, Rua Prof. Francisco Degni, 55 – Quitandinha - Araraquara, SP, Brazil - CEP 14800-060.

E-mail addresses: lia-marcondes@hotmail.com (L.M. Marcondes), marc.dussauze@u-bordeaux.fr (M. Dussauze).

materials such as lithium niobate LiNbO_3 are commonly used for optical signal processing and nonlinear frequency conversion [34] but require complex fabrication and predetermined design of crystalline materials that prevents future applications such as fiber optics, for example. NLO properties induced by thermal poling in germanate glasses has not been much explored. Recently, $70\text{GeO}_2\text{-}20\text{Ta}_2\text{O}_5\text{-}10\text{Na}_2\text{O}$ glass composition has been reported with a $\chi^{(2)}$ susceptibility of 0.3 pm/V [35]. For niobium matrices, the $50\text{GeO}_2\text{-}25\text{Nb}_2\text{O}_5\text{-}25\text{K}_2\text{O}$ [36] and $52\text{GeO}_2\text{-}28\text{Nb}_2\text{O}_5\text{-}20\text{K}_2\text{O}$ [29] glasses were described with 0.003 and 0.6 pm/V values, respectively.

In this paper, besides studying the effect of sodium and niobium contents on the NLO response of $\text{GeO}_2\text{-Nb}_2\text{O}_5\text{-Na}_2\text{O}$ glasses with up to 25mol% of Nb_2O_5 , the effect of the applied voltage during treatment was investigated. The polarization mechanisms were identified and discussed in detail, based on structural, Na-depletion thickness and SHG data. It has revealed a significant difference from classical models predictions which could be related to a strong influence of the negative charge motions mechanisms on the poling process efficiency. Finally, a successful test of microstructure design using an electrode structured by laser irradiation was demonstrated.

2. Experimental part

$(100\text{-x-y})\text{GeO}_2\text{-xNb}_2\text{O}_5\text{-yNa}_2\text{O}$ glasses with $x = 15, 20$ and 25 mol% and $y = 10$ and 15 mol% were synthesized using conventional melt-quenching and the glass compositions of the ternary system are described in Table 1. The samples were labeled as xNb_yNa , with x and y according to the molar compositions. The glasses were prepared using high purity analytical grade chemicals. The raw materials were GeO_2 (Fox-Chemicals 99.999 %), Nb_2O_5 (Alfa Aesar 99.9985 %) and Na_2CO_3 (Alfa Aesar 99.95 %). A batch of 15 g of raw materials was homogenized in a mortar and melted in a pure Pt crucible at 1500°C for 1 h. The melt was cast into a stainless-steel mold and then annealed at 500°C for 6 h to release internal mechanical stress. The samples were cut and optically polished using alumina suspensions with particle sizes of 20, 9, and 3 μm . The pictures of all samples are shown in the Fig. 1 inset.

For thermal poling treatment, a piece of silicon wafer was used as cathode and a soda-lime silicate glass ($0.5 \times 0.5 \times 0.1 \text{ cm}^3$) with deposited Pt film of 100 nm was used as anode (the anode was covered by a gold conductive thin film to ensure conductivity). The system was assembled using the cathode, a borosilicate coverslip to preserve the optical quality of the sample at the cathode side, the sample and finally the anode; the system was pressed with springs. Thermal poling was performed under a flow of N_2 atmosphere at $6 \text{ L}\cdot\text{min}^{-1}$ at 265°C using a heating rate of $15^\circ\text{C}/\text{min}$. Once the temperature is stabilized, DC voltages (900, 1200 or 1500 V) were applied with a rate of 300 V/min for 30 min. After this time, the heating system was turned off, with the direct current (DC) field remaining until the temperature was close to room temperature. The optical absorption spectra were recorded using an Agilent Cary 5000 spectrophotometer in the wavelength region 200–2500 nm and Bruker Equinox 55 in the wavelength region 2500–25,000 nm. DSC analysis were obtained employing a DSC calorimeter STA 449 F3 Jupiter from Netzsch in the temperature range of 200 to 1000°C , using Pt crucibles under a flow of N_2 atmosphere at $50 \text{ cm}^3\cdot\text{min}^{-1}$ with a heating rate of $10^\circ\text{C}\cdot\text{min}^{-1}$. Linear refractive indices were measured using Brewster's angle method at 532, 639, 785 and 935 nm and the dispersion of the indices fitted by a Cauchy fit [37]. Density

measurements were determined by Archimedes method using diethylphthalate at room temperature. Micro-Raman and micro-SHG correlative measurements were collected using a modified Jobin-Yvon Horiba-HR800 spectrometer equipment with a laser operating at 532 nm for Raman and a picosecond pulse laser at 1064 nm for SHG measurements [35]. Measurements were carried out on the surface and on the cross-section of the poled glasses. The objective 100x with a numerical aperture of 0.9 was used for Raman and SHG measurements. IR spectra were recorded by IR reflectance on a Fourier Vertex 70 V spectrometer with 200 scans and 2 cm^{-1} of spectral resolution, the absorbance spectra were calculated by the Kramers-Krönig analysis [38]. The Secondary ion mass-spectrometry (SIMS) were performed on a PHI Adept 1010 dynamic SIMS system. This technique consists of bombarding a surface with beams of ions and the ionized material is analyzed by a mass spectrometer to determine its composition. In this way, the qualitative distribution of the elements was analyzed, and the etching rate was calculated considering the depth of the crater measured by optical profilometry. Finally, the second order nonlinear optical susceptibilities ($\chi^{(2)}$) were quantified using the Maker fringes technique in transmission mode using incident nanosecond laser at 1550 nm. θ -scan and ψ -scan measurements were made as a function of the incident angle with fixed harmonic polarization p (horizontally) or s (vertically); or as a function of the polarization of the incident beam with fixed incident angle and fixed polarization at the analyzer, respectively [35]. Quartz z-cut plate was used as reference for the calibration of the SHG setup and simulated data from general matrix formulation of linear and nonlinear optical responses [39].

3. Results

$\text{GeO}_2\text{-xNb}_2\text{O}_5\text{-yNa}_2\text{O}$ ternary glass compositions were obtained by varying the sodium and niobium content. The niobium insertion limit is due to the low Nb_2O_5 solubility in the germanate liquid phase resulting in a liquid-liquid phase separation and spontaneous crystallization of the melt under cooling. The addition of 15 mol% of Na_2O improves the Nb_2O_5 solubility in the germanate matrix up to 25 mol% of Nb_2O_5 . This content of 25 mol% of Nb_2O_5 is higher than previously reported for alkali germanate glasses with 10mol% of potassium oxide [32]. Fig. 1 illustrates the wide transmission window from 0.4 to $5.2 \mu\text{m}$ with high transparency of around 80 % with two absorption bands at around 2.9 μm and 4.3 μm attributed to the vibrations of Ge-O-H bond [40].

Fig. 2 presents the refractive index and thermal data of all samples and Table 1 summarizes these data together with density values. An almost linear increase in density, refractive index and glass transition temperature occurs with higher niobium content as demonstrated in Fig. 3. Comparing the 15Nb10Na and 15Nb15Na samples also leads to an increase in the density and refractive index. Both compositions are below the level described for the effect known as germanate anomaly effect to occur [41]. Furthermore, for these samples, not only does the sodium concentration increase, but the Nb/Ge ratio variation also occurs as shown in Table 1 and the niobium content may be responsible for the observed changes. However, the sodium addition clearly influences the thermal stability parameter against crystallization ($\Delta T = T_x - T_g$, where T_g is a glass transition temperatures and T_x is onset of crystallization, Table 1) which increases from 85°C to 134°C . Glasses with high thermal stability are interesting for optical fibers manufacturing because they can prevent crystallization processes in the manufacturing process for

Table 1

Nominal molar composition, optical properties, density, and thermal stability against crystallization of sodium niobium germanate glasses.

Sample	Molar composition	n (639 nm)	d (g.cm ⁻³)	Nb/Ge (at.%)	Na/(Nb+Ge) (at.%)	$T_x - T_g$ ($^\circ\text{C}$)
15Nb10Na	$75\text{GeO}_2\text{-}15\text{Nb}_2\text{O}_5\text{-}10\text{Na}_2\text{O}$	1.786	3.970	0.40	0.190	85
15Nb15Na	$70\text{GeO}_2\text{-}15\text{Nb}_2\text{O}_5\text{-}15\text{Na}_2\text{O}$	1.799	4.011	0.43	0.300	134
20Nb15Na	$65\text{GeO}_2\text{-}20\text{Nb}_2\text{O}_5\text{-}15\text{Na}_2\text{O}$	1.848	4.096	0.61	0.274	108
25Nb15Na	$60\text{GeO}_2\text{-}25\text{Nb}_2\text{O}_5\text{-}15\text{Na}_2\text{O}$	1.911	4.127	0.83	0.273	49

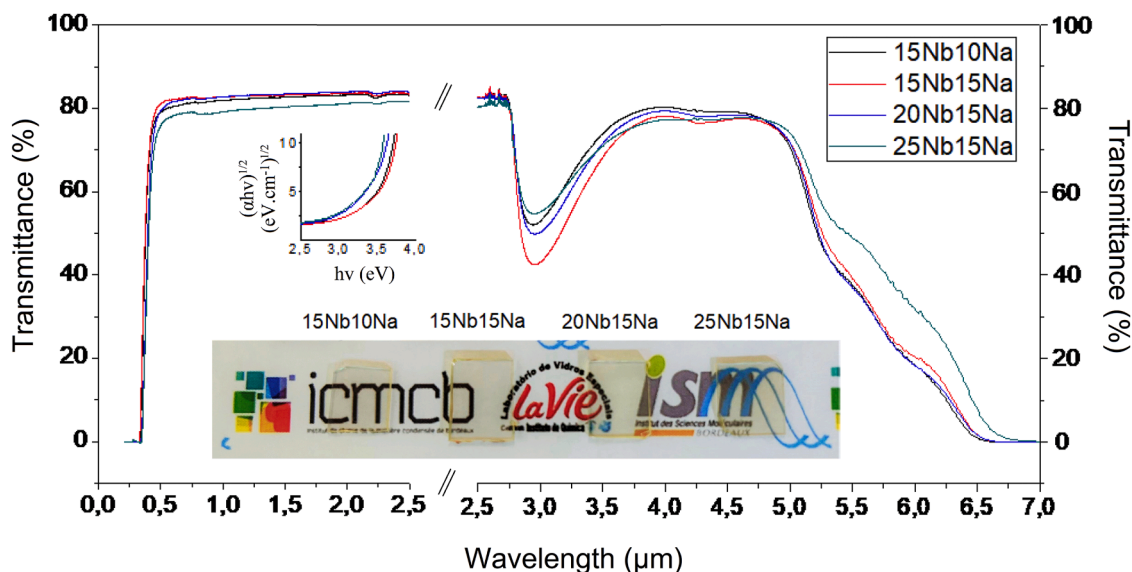


Fig. 1. Optical window of sodium niobium germanate glasses in the UV-Vis-MIR range and the pictures of all glass samples are shown in inset.

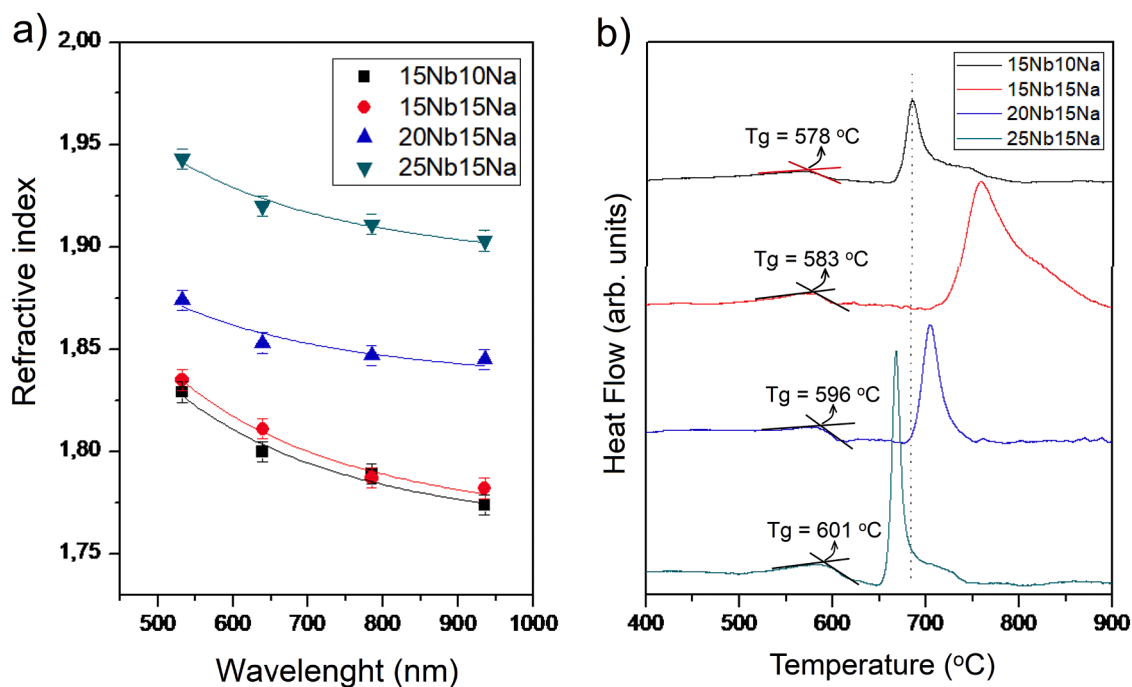


Fig. 2. (a) Refractive index dispersion of sodium niobium germanate glasses (the lines correspond to Cauchy fits) and (b) DSC curves.

fiber drawing.

All samples were subjected to thermal poling treatment at 265 °C and 1200 V and the 15Nb10Na sample at different DC voltages of 900, 1200 and 1500 V. Fig. 4(a) and (b) depict the thermal poling system assembly and the current curve as a function of thermal poling time, respectively. The current curve presented a typical profile of a successful thermal poling procedure [42]. Fig. 4(c) exhibits the SIMS profiles of 15Nb10Na sample after poling treatment at 900 V and describes the depth of the Na-depleted layer. As noted, the Na-depleted layer thickness is $2.42 \pm 0.05 \mu\text{m}$. The subanodic layer thicknesses of all samples are detailed in Table 2. The subanodic layer thickness almost doubles with increasing voltage from 900 to 1500 V and tends to increase with niobium content for the same voltage.

Fig. 5(a) and 5(b) present the infrared spectra of the samples before

and after poling. In these spectra, two main absorption regions attributed to vibrations in germanate glasses are observed. An absorption region around $800\text{--}900 \text{ cm}^{-1}$ assigned to antisymmetric stretching of GeO_4 tetrahedra containing non-bridging and bridging oxygens and a second absorption region around $420\text{--}600 \text{ cm}^{-1}$ related to a symmetric stretching modes of Ge-O-Ge bridging bonds [43]. The bands in the region of 300 and $580\text{--}800 \text{ cm}^{-1}$ are assigned to the bending and stretching Nb-O(-Nb) bond [44], respectively. In general, some modifications with the niobium and sodium content are observed in Fig. 5(a). The increase in niobium content leads to a clear increase in the band at 610 cm^{-1} assigned to the vibrational modes of the Nb-O-Nb bonds in NbO_6 units. Regarding the sodium content, a comparison between the 15Nb10Na and 15Nb15Na sample spectra shows that the sample with less sodium has a band around $800\text{--}900 \text{ cm}^{-1}$ wider in the 880 cm^{-1}

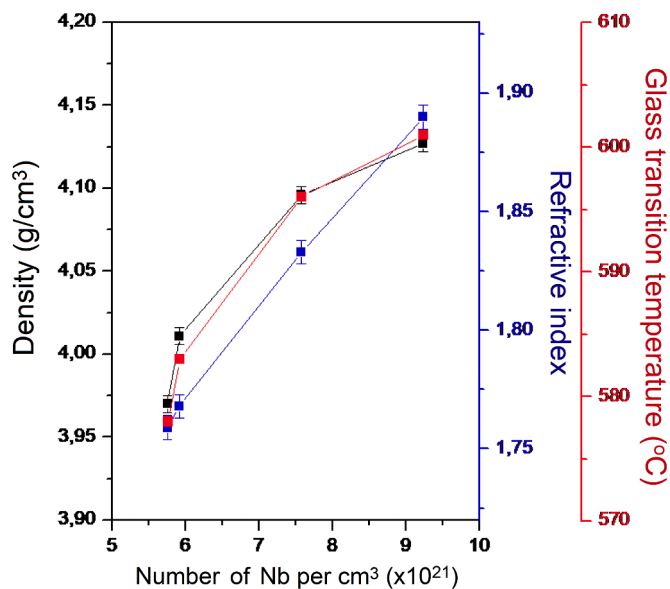


Fig. 3. Density, refractive index at 1550 nm and glass transition temperatures as a function of the niobium volume concentration.

region assigned to antisymmetric stretching of Ge-O bonds in Q_4 units without non-bridging oxygens (NBO), while the relative intensity of the band around 800 cm^{-1} assigned to antisymmetric stretching of Ge-O bonds in Q_3 units, i.e. with one NBO bond and three bonding oxygen bridging two germanium ions, decreases. The same trend but to a greater

magnitude is identified in the spectra of samples before and after thermal poling as shown in Fig. 5(b). A clear inversion between the bands at 805 and 880 cm^{-1} is demonstrated.

Raman spectra of the mixed niobium-germanate network are shown in Fig. 6(a) and have among their main bands: (1) a band around 470 cm^{-1} assigned to antisymmetric stretching of due to the Ge-O-Ge bond [45], (2) a band around 600 cm^{-1} attributed to vibrational modes of non-distorted NbO_6 units [46], like perovskite crystals constituted by a 3D network of corner-sharing NbO_6 units, (3) a band at 770 cm^{-1} associated with the vibrations of the distorted NbO_6 octahedra [47] and antisymmetric stretching of Nb-O(-Ge) bond [46] and finally, (4) a band at 880 cm^{-1} assigned to the NbO_6 with NBO bonds [48,49]. Furthermore, around 860 cm^{-1} a band referring to the asymmetric stretching of GeO_4 [50] also appears but is active mainly in the IR. Thus, the region at $600\text{--}800\text{ cm}^{-1}$ is attributed to vibrational modes of NbO_6 octahedra without NBO bonds where the lower distortion degree appears at lower frequency. As described in the IR data for samples with different niobium contents, the niobium addition increases the band at 600 cm^{-1}

Table 2

Post-poling Na-depleted layer thickness and second order optical susceptibility $\chi_{zzz}^{(2)}$ value of sodium niobium germanate glasses determined by Maker fringes.

Sample	Applied voltage (V)	Poled layer (μm)	$\chi_{zzz}^{(2)}$ (pm/V)
15Nb10Na	900	2.42 ± 0.05	0.42 ± 0.04
15Nb10Na	1200	3.22 ± 0.05	0.39 ± 0.04
15Nb10Na	1500	4.26 ± 0.05	0.33 ± 0.03
15Nb15Na	1200	3.31 ± 0.05	0.42 ± 0.04
20Nb15Na	1200	4.04 ± 0.05	0.60 ± 0.06
25Nb15Na	1200	3.95 ± 0.05	0.76 ± 0.08

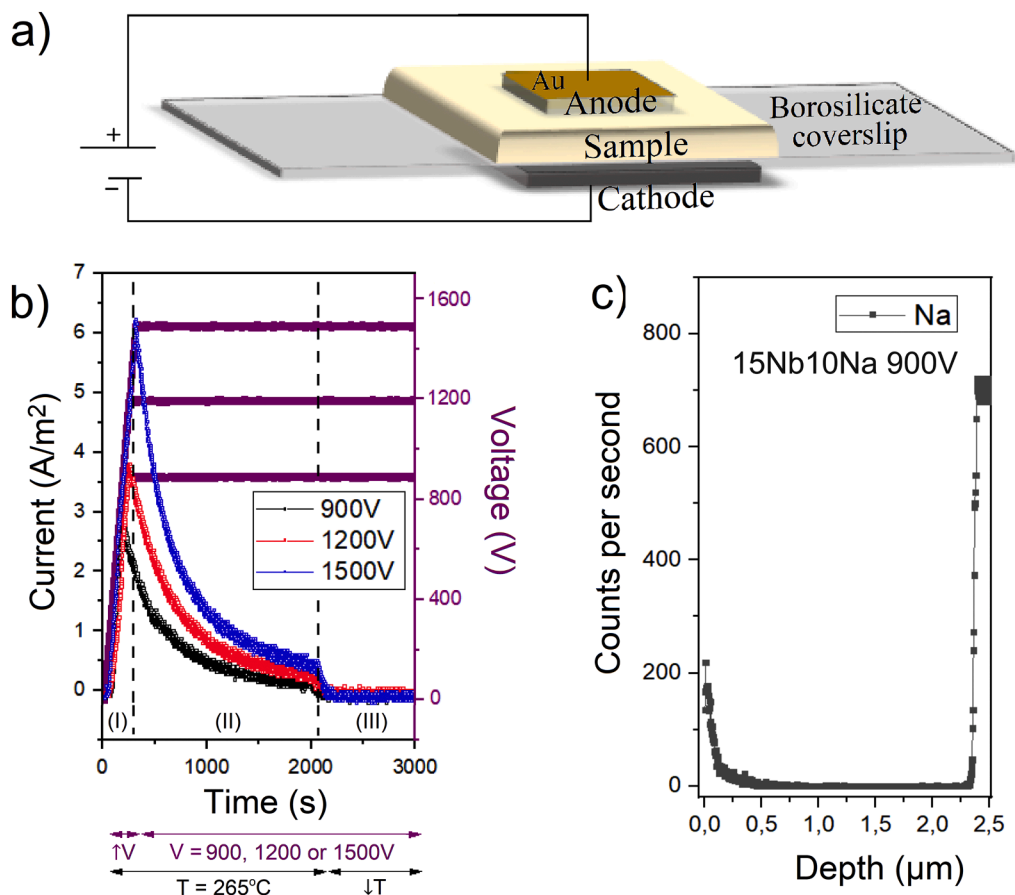


Fig. 4. (a) Thermal poling system assembly, (b) recorded voltage and current curves during thermal poling treatment and (c) SIMS depth profile after poling of sodium content in 15Nb10Na samples at 900 V.

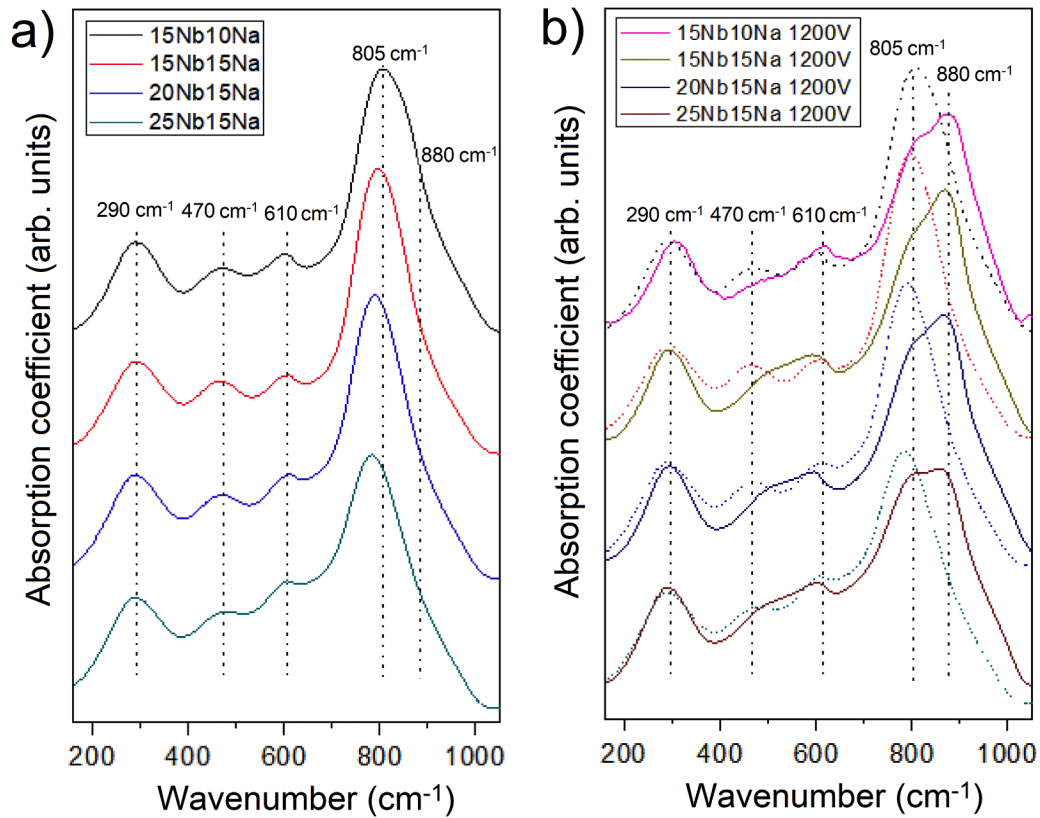


Fig. 5. Absorption coefficients obtained by the reflectance spectra Kramers-Krönig transformation of the samples (a) before and (b) after thermal poling of sodium niobium germanate glasses.

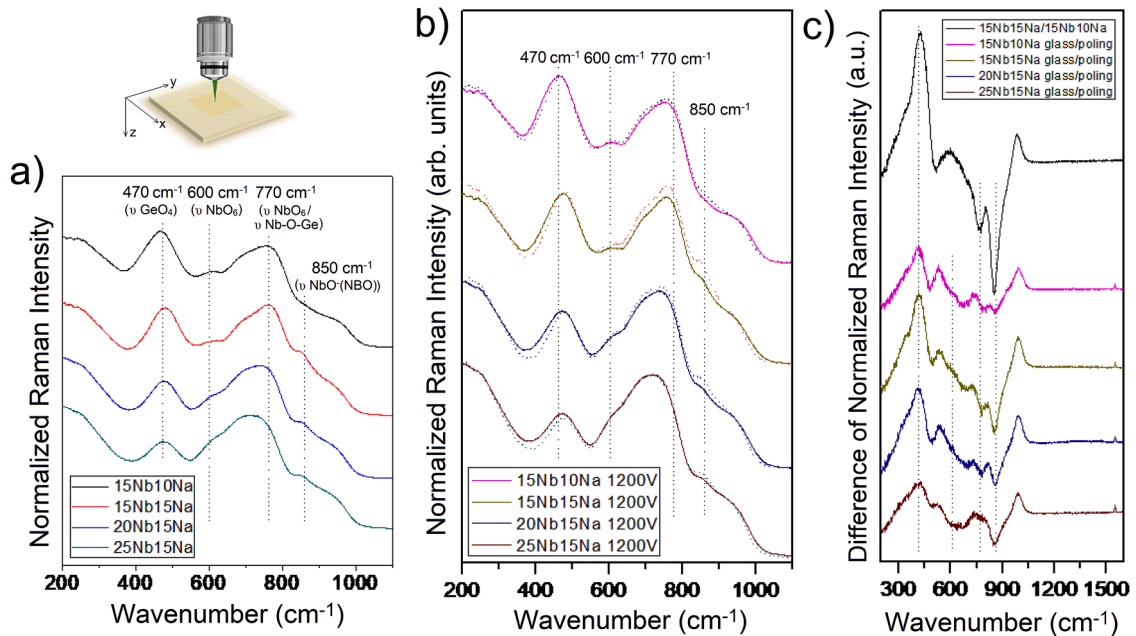


Fig. 6. Raman spectra top view of the samples (a) before and (b) after thermal poling; and (c) Raman spectra difference corresponding to the spectra of the highest sodium content glass (15Nb15Na) subtracted from the smallest content glass (15Nb10Na), and the others referring to the spectra of the glass without poling subtracted from the spectra of the poled zone.

due to the formation of interconnected NbO₆ units and, in the Raman spectra, there is an increase in the band around 600 cm⁻¹ and also a shift from 763 to 709 cm⁻¹ attributed to less and less deformed NbO₆ units. Finally, the spectra before and after thermal poling are shown in Fig. 6

(b). Fig. 6(c) presents the difference of normalized Raman intensity. Raman difference spectra between the 15Nb15Na and 15Nb10Na samples considering the decrease in sodium content (black line, Fig. 6c) was also inserted and has a similar profile with the Raman differences of the

samples before and after the poling treatment. In the Na-depleted sub-anodic microlayer spectra, a decrease occurs in the 770 and 850 cm^{-1} bands and an increase in the band around 460 cm^{-1} due to the shift from 471 to 459 cm^{-1} . Finally, a band at 1550 cm^{-1} appears exclusively in the anodic microlayer and is assigned to the symmetric stretching of molecular oxygen trapped in the matrix [32]. Fig. 7 reports the Raman data recorded on the cross-section of the poled 20Nb15Na sample. Raman maps demonstrate that the structural rearrangements occur exclusively at 4 μm thickness, which corresponds to the Na-depleted microregion detected by SIMS and described in Table 2.

In addition to structural modification, thermal poling treatment breaks the glass centrosymmetry inducing a second order optical response such as second harmonic generation (SHG). Fig. 8(a) and 8(b) illustrate the subanodic layer characterized in its cross-section by μ -SHG polarized microscopy with linear incident polarization oriented either along the Z and Y axis, respectively, and fixed analyzed polarization along Z axis for the backscattered SHG signal. These configurations were noted as I_{ZZ} and I_{YZ} , where the first and second letter refer to the configuration state of the incident light polarization and linear polarization of backscattered SHG signals, respectively. SHG intensity allows probing the second order susceptibility $\chi_{ZZ}^{(2)}$ and $\chi_{YZ}^{(2)}$, respectively. As shown in Fig. 8(c), the I_{ZZ}/I_{YZ} ratio is close to 9 ($\pm 10\%$) and fits the ratio between the terms $\chi_{ZZ}^{(2)} = 3\chi_{YZ}^{(2)}$. Fig. 8(d) shows the SHG intensity versus the incident polarization state obtained by macro-SHG response using a Maker fringes setup. The scans were labeled as Ψ -p and Ψ -s scans for horizontal and vertical SHG detection polarization, respectively. The electric field induced second harmonic (EFISH) model based on $C_{\infty v}$ local symmetry along the z axis was used to simulate all the data [32]. The EFISH simulation describes all the data very well. A slight discrepancy was observed for the maximum value of the Ψ -p scan,

nevertheless, one can consider that the SHG response is majority linked to an electrooptical origin. The $\chi^{(2)}$ values obtained from these analyzes are summarized in Table 2 and have an increase with niobium content from 0.42 to 0.76 pm/V and an unexpected decrease from 0.42 to 0.33 pm/V when the poling voltage increases from 900 to 1500 V. These values are not as high as for glasses containing higher levels of niobium, such as niobium borophosphate glasses with up to 48 mol% of Nb_2O_5 [51–54] or amorphous thin film in the Nb_2O_5 - Na_2O binary system [55]. However, the $\chi^{(2)}$ values of these samples are higher when compared to other germanate glasses. The sample with 25 mol% of Nb_2O_5 has a $\chi^{(2)}$ value twice as high as germanate glasses with 20 mol% of Ta_2O_5 [35] and also higher than another germanate glass with 28 mol% of Nb_2O_5 [29].

Finally, in order to demonstrate the promising potential of these samples for future microscale photonic applications, a poling treatment test on the 15Nb15Na sample using an ITO electrode microstructured by picosecond laser inscription was performed. Fig. 9(a) and (b) illustrate the microstructured surface by laser ablation on the electrode used as anode and a picture of the sample after poling treatment, respectively. The excellent resolution of the microlocalized SHG signal in the region in contact with the micromodified electrode can be observed in Fig. 8(c).

4. Discussion

As shown in Figs. 1 and 8, niobium germanate glasses have a spectral transmission up to 5200 nm and a SHG response induced by thermal poling. Although the NLO responses are less than in crystalline materials such as LiNbO_3 [56] or in niobium borophosphate glasses that allow a higher niobium content [54], niobium germanate glasses are highlighted for non-linear applications in the mid-IR region since they have

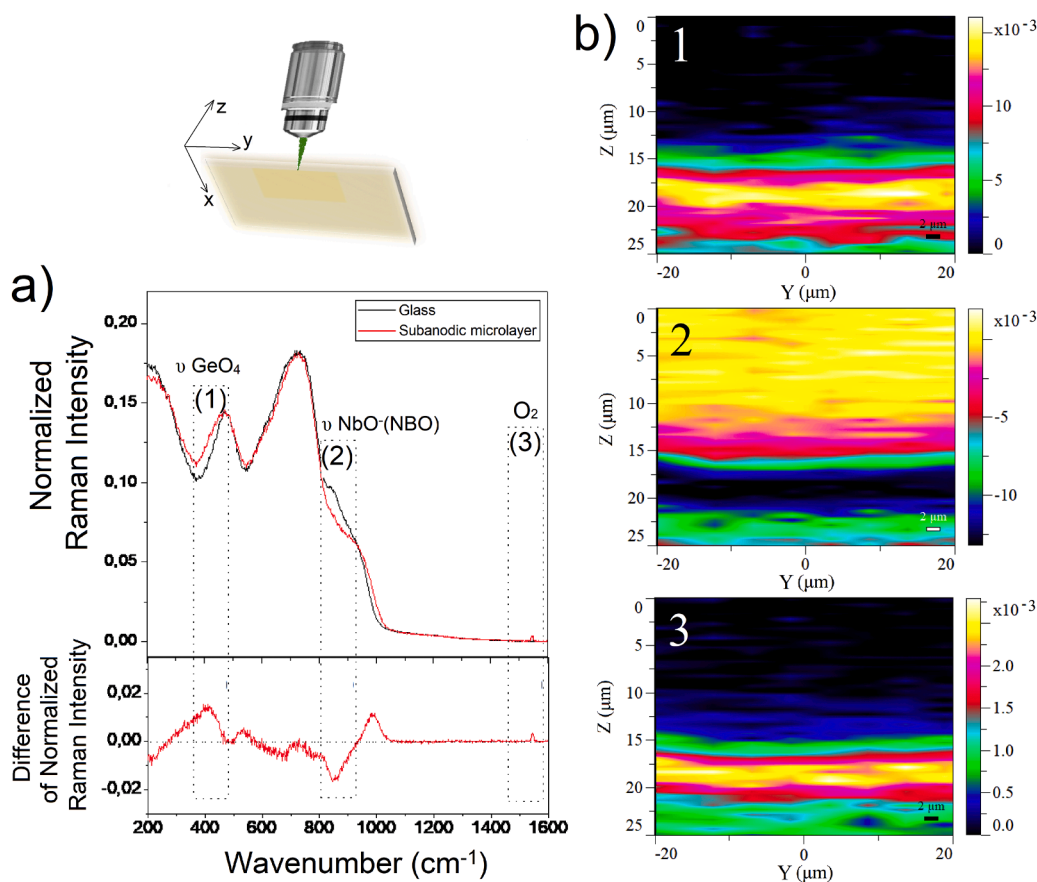


Fig. 7. (a) Raman spectra cross-section of 20Nb15Na sample in the anion sublayer where there was in contact with the electrode - in red - and the glass - in black, and (b) Raman intensity mapping of modes 1, 2 and 3 highlighted in a.

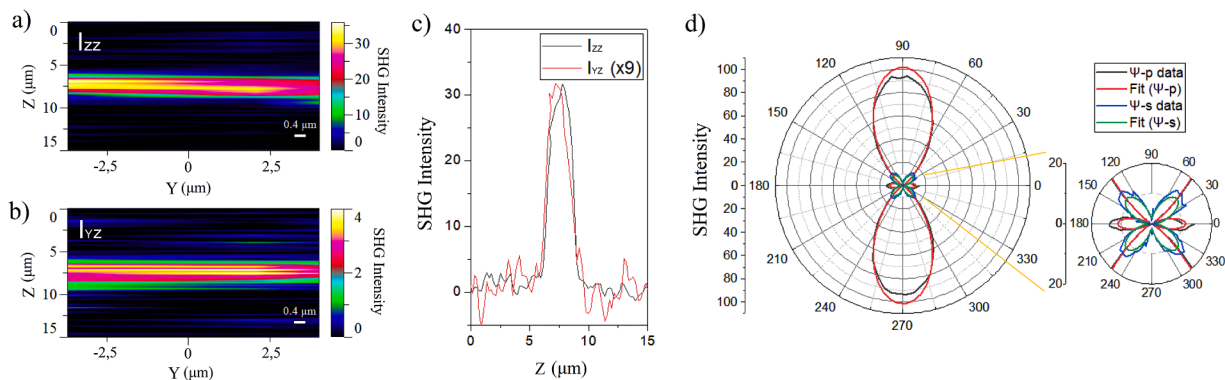


Fig. 8. (a) Micro-SHG maps, (b) comparison of SHG maps for different light polarization configurations and (c) macro-SHG measurements by Maker fringes and EFISH simulation.

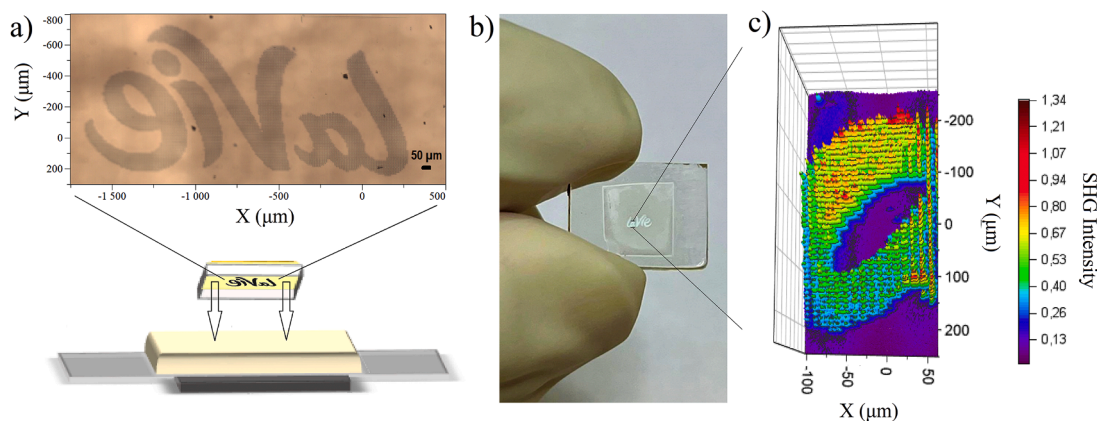


Fig. 9. (a) Optical micrographs of the surface of the structured ITO electrode, (b) picture of micromodified 15Nb15Na sample after poling treatment and (c) SHG Mapping realized on the modified surface with linearly polarized light perpendicular to the imprinted structure.

transparency in the mid-IR of the germanate matrix, are easy to synthesize and allow variation in the shape of the material as they are glass matrix. Alkaline niobium germanate glasses are described as a mixed $\text{GeO}_4\text{-NbO}_6$ network leading to the formation of NbO_6 clusters with increasing niobium content [57]. This NbO_6 polyhedra network was confirmed in the IR and Raman data of Figs. 5(a) and 6(a) due to the increase in the band around 600 cm^{-1} assigned to the stretching of Nb-O-Nb bonds in NbO_6 units without NBO connections with niobium content. Furthermore, in the Raman spectra, an evident shift of the band from 763 to 709 cm^{-1} was identified due to the formation of less-distorted NbO_6 polyhedra and decrease in the extension of the mixed $\text{GeO}_4\text{-NbO}_6$ network through Nb-O-(Ge) bonds. These structural modifications demonstrate a higher overall network connectivity with niobium content and are the main factors for the changes in certain properties, such as an increase in density [58], in the glass transition temperature [29], and in the NLO response [31] and finally a decrease in the parameters of thermal stability against crystallization [32].

After thermal poling, a sodium depletion on the surface of niobium germanate glasses formed a microlayer of 2.4 to $4.0\text{ }\mu\text{m}$ probed by time-of-flight secondary ion mass spectrometry (TOF-SIMS) and is the main cause of structural rearrangements in the subanodic layer. Structural modifications were investigated inside and outside of the Na-depletion microlayer and also between 15Nb15Na and 15Nb10Na samples with different sodium contents. As expected, both the decrease in sodium in the 15Nb15Na and 15Nb10Na bulk samples without thermal poling and the sodium depletion in the microlayer after poling treatment follow the same trend of structural rearrangement: a change in the ratio between bridging and non-bridging oxygens (NBO) bonds linked to variation in sodium contents. In the IR spectra of Fig. 5(b), the decrease in NBO

bonds is evidenced by the reduction of the band at 800 cm^{-1} and by the increase at 880 cm^{-1} assigned to $\nu\text{ Ge-O}^-$ and $\nu\text{ Ge-O-Ge}$, respectively. A conversion from $\text{Q}^3\text{ GeO}_4$ units to $\text{Q}^4\text{ GeO}_4$ units occurs, and this effect is more pronounced in the post-poling Na-depletion microlayer than in samples with different sodium contents without treatment, since this subanodic region is empty of sodium. In the Raman spectra of Figure 69 (c), the decrease in NBO bonds is evidenced by the decrease in the band around 850 cm^{-1} , which in this case mainly refers to the vibration of terminal Nb-O⁻ bonds. Furthermore, in the sodium-empty subanodic microlayer, a band decrease at 770 cm^{-1} and band shift at 465 cm^{-1} are identified and occur due to the formation of a glass network with less interconnections with Nb-O-Ge bonds and greater connections between GeO_4 - and NbO_6 -rich amorphous region: (1) the band at 770 cm^{-1} is assigned to Nb-O-Ge bonds and deformed NbO_6 polyhedra and (2) the band shift around 470 cm^{-1} occurs due to the increase in the average value of the intertetrahedral Ge-O-Ge bond angle [59]. One has to point out that the formation of this amorphous matrix with a high content of Ge-O-Ge and Nb-O-Nb linkages without NBO bonds is only achieved after thermal poling treatment, since traditional melt-quenching method results in a spontaneous crystallization due to low Nb_2O_5 solubility in the germanate liquid phase. This highly connected network and amorphous phase separation have also been reported for tantalum germanate glasses [35]. Finally, Fig. 7 shows that the band at 1550 cm^{-1} is limited in the subanodic region and refers to the presence of trapped molecular oxygen after poling treatment with a blocking anode-electrode configuration [25]. This molecular oxygen results from the sodium ions departure and the rearrangement of the remaining glass network.

During thermal poling, a DC bias is applied across the heated sample and the current measured as a function of treatment time was plotted in

Fig. 4(b). This Figure shows that the current (I) increases until the voltage is held constant, (II) decreases when the voltage is held constant and (III) decreases again when the heater is turned off. After the last step, the DC bias is removed only when a sample is brought back to room temperature to prevent charge mobility in the glass network. In general, in stage I, the dissociation process of Na^+ ions starts. In stage II, a depletion layer in Na^+ ions is formed and the decrease in current occurs due to the gradual decrease in the dissociation process, forming the sodium free layer which exhibits a low ionic conductivity [60]. Finally, in stage III there is a sudden drop in current when the temperature is turned off [42]. This mobile cations depletion, confirmed by TOF-SIMS data and described structural changes, leads to a volumetric space charge, and allows the implementation of a static electrical field in the subanodic microlayer. Fig. 8 demonstrates the presence of SHG signal in the NLO-active layer and the thickness of the detected SHG signal region is consistent with the sodium depletion of around 4 μm obtained by TOF-SIMS analysis. Fig. 8(d) shows the fit of the SHG data considering the electric field induced second harmonic (EFISH) model and confirms the electrooptical origin of the NLO signal. Thus, in this case, both the third-order susceptibility ($\chi^{(3)}$) of an isotropic material and the magnitude of the permanent static electrical field are relevant to interpret the NLO response. Regarding the SHG data on different glass compositions for the same poling parameters, higher niobium contents promoted an increase in the poling induced $\chi^{(2)}$ susceptibility. This occurs due to the expected increase in $\chi^{(3)}$ susceptibility which can be attributed to the higher polarizability of d^0 transition ions such as niobium but also to the niobate structural arrangement forming a 3D network of octahedral NbO_6 units known to enhance the third order optical properties in various oxide glasses [61].

In the case of the increase of applied voltages for the same niobium content (15Nb10Na sample) an unexpected decrease in the $\chi^{(2)}$ values was identified and will be discussed in detail below. Thermal poling causes a depletion of positive charges and consequently an excess of negative charges in the subanodic microlayer. In the case of blocking anode configuration, i.e. prohibiting the possibility of positive charge injection in the poled glass, the compensation mechanisms are dictated by the motion of negative charge carriers from the glass network. These polarizations mechanisms are known to induce structural rearrangements and formation of neutral isolated species trapped in the glass matrix upon oxidation reactions [27]. In this study, FTIR and Raman data confirm the structural changes and Raman mapping of Fig. 7(b) demonstrates the O_2 formation exclusively in the subanodic microlayer. Two main mechanisms have been proposed in the literature to explain O_2 generation after thermal poling in blocking anode configuration. [24]. The first process is described by the electronic conductivity in the region depleted of positive ions and is caused by the self-healing dielectric breakdown that allows electrons hopping between oxygen sites without the need for motion of oxygen ions [25,26]. In this case, a series of intermediate reactions occur involving the recombination of all adjacent pairs of NBO bonds, peroxide radicals and finally leading to the formation of molecular oxygen and resulting in an increase in the degree of the glass matrix polymerization [25,29]. The second process is related to anionic conduction [25]. In this case, the polymerization of the structure occurs due to oxidation reactions within the space charge layer that led to sodium release: $2[\text{Ge-O}^-\dots\text{Na}^+] \rightarrow \text{Ge-O-Ge} + \text{O}^{2-} + 2\text{Na}^+$, and formation of O_2 from oxygen anions: $\text{O}^{2-} \rightarrow \frac{1}{2}\text{O}_2 + 2\text{e}^-$ [29]. In the case of our glass samples, both charge recombination mechanisms can be expected, and no additional observation allowed concluding on one predominant process. Nevertheless, as shown in Table 2, an unexpected decrease in $\chi^{(2)}$ was identified for the 15Nb10Na sample with increasing applied voltages. According to a classical model describing the formation of a polarized layer in glassy materials, if the applied voltage increase, the strength of the induced static electric field in the space charge layer is expected to increase and the thickness of the poled layer should vary according to the square root of the applied voltage [27]. This trend is clearly not observed in this study, as shown in Table 2. The sodium

depleted layer thickness increases almost linearly with the applied field and the induced EFISH $\chi^{(2)}$ susceptibility decreases. In this case, this unusual tendency may be related to an increase of the negative charge carriers mobility with the applied voltage. In a previous work, it was necessary to consider an exponential growth of the negative charge carrier mobility with the magnitude of the local electric field to model charge motions during a poling process of an ionic glassy matrix. This model considers constant activation energy and thus mobilities of the charge carriers. In this perspective, a variation in the negative charge motion activation energy may be the cause of the model divergence. If the mobility of negative charge carriers (oxygen anions or electrons) varies with the applied voltage, a strong increase in applied voltage may have led to a significant decrease in the activation energy of negative charge motion facilitating sodium compensation and allowing for greater sodium migration. This phenomenon is consistent with that described for insulating materials under a high electric field, where activation energy and electrical conduction are dependent on the applied field [61] and the effect of high voltage described by the Poole-Frenkel effect [62]. In this way, a Na-depleted thickness greater than expected can then be explained together with a decrease of the EFISH $\chi^{(2)}$ susceptibility, since a greater space charge layer thickness results in a decrease in the induced static electric field strength and consequently in the second order optical response.

5. Conclusion

Structural and optical properties were investigated in sodium niobium germanate glasses before and after thermal poling. The increase in niobium content in glass germanate led to the formation of NbO_6 polyhedra with a coordination number greater than GeO_4 units, increasing connectivity in the mixed covalent niobium-germanate chains, and consequently an increase in glass transition temperature and density of the material. Furthermore, the niobium content improves the NLO response in the subanodic layer after poling treatment, since increasing the amount of highly polarizable NbO_6 units improves the $\chi^{(3)}$ susceptibility, which is directly related to the $\chi^{(2)}$ susceptibility, according to the EFISH model. Finally, regarding the increase in voltage in the thermal poling, an unexpected linear increase in the thickness of the NLO-active space charge layer and a decrease in $\chi^{(2)}$ susceptibility was observed. A different response from the classical space charge formation model occurs due to the decrease in the activation energy of negative charge motion in the material under high tensions. In this sense, the decrease in this activation energy facilitates sodium compensation and allows greater migration of sodium ions, which consequently reduces the magnitude of the induced electric field by thermal poling.

CRedit authorship contribution statement

Lia Mara Marcondes: Formal analysis, Investigation, Writing – original draft, Writing – review & editing. **Juliane Resges Orives:** Investigation, Validation, Writing – review & editing. **Frederic Adamitez:** Investigation, Writing – review & editing. **Gael Yves Poirier:** Conceptualization, Validation, Writing – review & editing. **Thierry Cardinal:** Validation, Writing – review & editing. **Marc Dussauze:** Conceptualization, Investigation, Formal analysis, Writing – review & editing, Supervision. **Marcelo Nalin:** Conceptualization, Investigation, Resources, Writing – review & editing, Supervision.

Declaration of competing interest

The authors declare that they have no known competing financial interests or personal relationships that could have appeared to influence the work reported in this paper.

Data availability

Data will be made available on request.

Acknowledgments

The authors acknowledge the financial supports from São Paulo Research Foundation Agency, FAPESP (grants n° 2013/07793-6, 2019/19609-1, 2020/01786-1, 2021/11494-0). The Raman and SHG experiments were conducted using the SIV platform at the University of Bordeaux founded by the FEDER and the Region Aquitaine. This project has also received funding from the European Union's Horizon 2020 research program under the Marie SkłodowskaCurie grant agreement no. 823941 (FUNGLASS), New Aquitaine region (Grant 2016–1R10107) and IDEX Bordeaux (Research Program GPR Light).

References

- W. Blanc, Y.G. Choi, X. Zhang, M. Nalin, K.A. Richardson, G.C. Righini, M. Ferrari, A. Jha, J. Massera, S. Jiang, J. Ballato, L. Petit, The past, present and future of photonic glasses: a review in homage to the united nations international year of glass 2022, *Prog. Mater. Sci.* 134 (2023) 101084, <https://doi.org/10.1016/j.pmatsci.2023.101084>.
- V.S. Shiryayev, M.F. Churbanov, Recent advances in preparation of high-purity chalcogenide glasses for mid-IR photonics, *J. Non-Cryst. Solids* 475 (2017) 1–9, <https://doi.org/10.1016/j.jnoncrysol.2017.09.021>.
- V. Ghergia, New materials for optoelectronic devices, *Ceram. Int.* 19 (1993) 181–190, [https://doi.org/10.1016/0272-8842\(93\)90039-T](https://doi.org/10.1016/0272-8842(93)90039-T).
- W.H. Kim, V.Q. Nguyen, L.B. Shaw, L.E. Busse, C. Florea, D.J. Gibson, R.R. Gattass, S.S. Bayya, F.H. Kung, G.D. Chin, R.E. Miklos, I.D. Aggarwal, J.S. Sanghera, Recent progress in chalcogenide fiber technology at NRL, *J. Non-Cryst. Solids* 431 (2016) 8–15, <https://doi.org/10.1016/j.jnoncrysol.2015.03.028>.
- V.G. Ta'eed, N.J. Baker, L. Fu, K. Finsterbusch, M.R.E. Lamont, D.J. Moss, H. C. Nguyen, B.J. Eggleton, D.Y. Choi, S. Madden, B. Luther-Davies, Ultrafast all-optical chalcogenide glass photonic circuits, *Opt. Express* 15 (15) (2007) 9205–9221, <https://doi.org/10.1364/OE.15.009205>.
- M. Tang, Y. Ma, S. Wen, G. Du, J. Chen, X. Li, S. Lv, S. Zhou, Gallosilicate glass and fiber for radiation detection, *J. Am. Ceram. Soc.* 106 (6) (2023) 3438–3445, <https://doi.org/10.1111/jace.19058>.
- Z. Qiu, S. Dai, C. Liu, W. Wu, Z. Xu, Y. Wang, Y. Fu, Novel Ge-As-Se chalcogenide glass for potential high Brillouin gain coefficient of fiber, *Ceram. Int.* 49 (10) (2023) 16433–16439, <https://doi.org/10.1016/j.ceramint.2023.02.004>.
- S. Kang, Z. Huang, W. Lin, D. Yang, J. Zhao, X. Qiao, X. Xiao, S. Xu, J. Qiu, J. Du, G. Dong, Enhanced single-mode fiber laser emission by nano-crystallization of oxyfluoride glass-ceramic cores, *J. Mater. Chem. C* 7 (2019) 5155–5162, <https://doi.org/10.1039/C9TC01170F>.
- S. Danto, F. Désévéday, Y. Petit, J.-C. Desmoulin, A.A. Khalil, Marc Dussauze C. Strutynski, F. Smektala, T. Cardinal, L. Canioni, Photowritable silver-containing phosphate glass ribbon fibers, *Adv. Opt. Mater.* 4 (1) (2016) 162–168, <https://doi.org/10.1002/adom.201500459>.
- X. Wang, Y. Tian, Y. Zhang, D. Tang, B. Li, J. Zhang, S. Xu, Effect of Al(PO₃)₃, NaF, and SrF₂ on structure and properties of fluorophosphate glass, *J. Non-Cryst. Solids* 602 (2023) 122089, <https://doi.org/10.1016/j.jnoncrysol.2022.122089>.
- M. Ghanad, N. Akrami, P. Keil, H. Bradtmüller, M.R. Hansen, J.V. Khaki, S. M. Beidokhti, Single-step solution combustion synthesis of porous 1393-B3 glass powders and structural characterization via solid-state NMR spectroscopy, *Ceram. Int.* 49 (9) (2023) 14689–14701, <https://doi.org/10.1016/j.ceramint.2023.01.061>.
- S. Das, P. Priyadarshini, D. Alagarasan, S. Vardhrajperumal, R. Ganesan, R. Naik, Role of tellurium addition on the linear and non-linear optical, structural, morphological properties of Ag_{60-x}Se₄₀Te_x thin films for nonlinear applications, *J. Am. Ceram. Soc.* 105 (5) (2022) 3469–3484, <https://doi.org/10.1111/jace.18361>.
- A.M. Abd-Elnaiem, A.Z. Mahmoud, S. Moustafa, Structural and optical properties of thermally evaporated and annealed Ge₂₀Se₇₆Sn₄ thin films, *Opt. Mater.* 111 (2021) 110607, <https://doi.org/10.1016/j.optmat.2020.110607>.
- Z. Rajaofara, P. Leproux, M. Dussauze, A. Tonello, V. Rodriguez, L. Karam, H. Kano, J.-R. Duclère, V. Couderc, Mapping the second and third order nonlinear susceptibilities in a thermally poled microimprinted niobium borophosphate glass, *Opt. Mater. Express* 11 (10) (2021) 3411–3420, <https://doi.org/10.1364/OME.433809>.
- H.-Y. Chen, Y.-S. Lin, Influence of multi-energy boron difluoride implantation on the second-harmonic generation of thermally poled fused silica, *Opt. Mater.* 109 (2020) 110451, <https://doi.org/10.1016/j.optmat.2020.110451>.
- X. He, B. Poumellec, Q. Liu, F. Brisset, M. Lancry, One-step photoinscription of asymmetrically oriented fresnoite-type crystals in glass by ultrafast laser, *Opt. Lett.* 39 (18) (2014) 5423–5426, <https://doi.org/10.1364/OL.39.005423>.
- E.O. Smetanina, B. Chimier, Y. Petit, A. Royon, T. Cardinal, L. Canioni, G. Duchateau, Laser writing of nonlinear optical properties in silver-doped phosphate glass, *Opt. Lett.* 42 (9) (2017) 688–1691, <https://doi.org/10.1364/OL.42.001688>.
- Y. Li, L. Wang, M. Liao, L. Zhang, W. Bi, T. Xue, Y. Liu, R. Zhang, Y. Ohishi, Suspended-core fluoride fiber for broadband supercontinuum generation, *Opt. Mat.* 96 (2019) 109281, <https://doi.org/10.1016/j.optmat.2019.109281>.
- I. Alamgir, F. St-Hilaire, M. Rochette, All-fiber nonlinear optical wavelength conversion system from the C-band to the mid-infrared, *Opt. Lett.* 45 (4) (2020) 857–860, <https://doi.org/10.1364/OL.386272>.
- S. Ohara, H. Masai, Y. Takahashi, T. Fujiwara, Y. Kondo, N. Sugimoto, Space-selectively crystallized fiber with second-order optical nonlinearity for variable optical attenuation, *Opt. Lett.* 34 (7) (2009) 1027–1029, <https://doi.org/10.1364/OL.34.001027>.
- G. Wallis, D.I. Pomerantz, Field assisted glass-metal sealing, *J. Appl. Phys.* 40 (1969) 946, <https://doi.org/10.1063/1.1657121>.
- F. de Lucia, P.J.A. Sazio, Thermal poling of optical fibers: a numerical history, *Micromachines* 11 (2) (2020) 139, <https://doi.org/10.3390/mi11020139>.
- R.A. Myers, N. Mukherjee, S.R.J. Brueck, Large second-order nonlinearity in poled fused silica, *Opt. Lett.* 16 (1991) 1732–1734, <https://doi.org/10.1364/OL.16.001732>.
- M. Dussauze, T. Cremoux, F. Adamietz, V. Rodriguez, E. Fargin, G. Yang, T. Cardinal, Thermal poling of optical glasses: mechanisms and second-order optical properties, *Int. J. Appl. Phys. Sci.* 3 (4) (2012) 309–320, <https://doi.org/10.1111/ijag.12001>.
- M. Dussauze, V. Rodriguez, A. Lipovskii, M. Petrov, C. Smith, K. Richardson, T. Cardinal, E. Fargin, E.I. Kamitsos, How does thermal poling affect the structure of soda-lime glass, *J. Phys. Chem. C* 114 (29) (2010) 12754–12759, <https://doi.org/10.1021/jp1033905>.
- U.K. Krieger, W.A. Lanford, Field assisted transport of Na⁺ ions, Ca²⁺ ions and electrons in commercial soda-lime glass I: experimental, *J. Non-Cryst. Solids* 102 (1988) 50–61, [https://doi.org/10.1016/0022-3093\(88\)90112-3](https://doi.org/10.1016/0022-3093(88)90112-3).
- M. Dussauze, E.I. Kamitsos, E. Fargin, V. Rodriguez, Structural rearrangements and second-order optical response in the space charge layer of thermally poled sodium-niobium borophosphate glasses, *J. Phys. Chem. C* 111 (39) (2007) 14560–14566, <https://doi.org/10.1021/jp074335f>.
- G. Guimbretière, M. Dussauze, V. Rodriguez, E.I. Kamitsos, Correlation between second-order optical response and structure in thermally poled sodium niobium-germanate glass, *Appl. Phys. Lett.* 97 (2010) 171103, <https://doi.org/10.1063/1.3506501>.
- H. Zeghlache, M. Guignard, A. Kudlinski, Y. Quiquempois, G. Martinelli, V. Nazabal, F. Smektala, Stabilization of the second-order susceptibility induced in a sulfide chalcogenide glass by thermal poling, *J. Appl. Phys.* 101 (2007) 084905, <https://doi.org/10.1063/1.2719008>.
- W.D. Dumbaugh, Infrared transmitting germanate glasses, *SPIE Emerg. Optic. Mater.* 297 (1982) 80–85, <https://doi.org/10.1117/12.932488>.
- D. Manzani, T. Gualberto, J.M.P. Almeida, M. Montesso, C.R. Mendonça, V.A. G. Rivera, L. de Boni, M. Nalin, S.J.L. Ribeiro, Highly nonlinear Pb₂O₇-Nb₂O₅ glasses for optical fiber production, *J. Non-Cryst. Solids* 443 (2016) 82–90, <https://doi.org/10.1016/j.jnoncrysol.2016.04.01>.
- L.M. Marcondes, S. Maestri, B. Souza, R.R. Gonçalves, F.C. Cassanjes, G.Y. Poirier, High niobium oxide content in germanate glasses: thermal, structural, and optical properties, *J. Am. Ceram. Soc.* 101 (2018) 220–230, <https://doi.org/10.1111/jace.15215>.
- D. Munoz-Martin, A.R. de La Cruz, J.M. Fernandez-Navarro, C. Domingo, J. Solis, J. Gonzalo, Structural origin of the nonlinear optical properties of lead niobium germanate film glasses, *J. Appl. Phys.* 110 (2011) 023522, <https://doi.org/10.1063/1.3608172>.
- M.R. Karim, N. Al Kayed, M.R. Hossain, B.M.A. Rahman, Study of low-peak-power highly coherent broadband supercontinuum generation through a dispersion-engineered Si-rich silicon nitride waveguide, *Appl. Opt.* 59 (20) (2020) 5948–5956, <https://doi.org/10.1364/AO.395705>.
- G. Poirier, M. Dussauze, V. Rodriguez, F. Adamietz, L. Karam, T. Cardinal, E. Fargin, Second harmonic generation in sodium tantalum germanate glasses by thermal poling, *J. Phys. Chem. C* 123 (43) (2019) 26528–26535, <https://doi.org/10.1021/acs.jpcc.9b0822>.
- Y. Benino, Y. Takahashi, T. Fujiwara, T. Komatsu, Second order optical non-linearity of transparent glass-ceramic materials induced by alternating field, *J. Non-Cryst. Solids* 345–346 (2004) 422–427, <https://doi.org/10.1016/j.jnoncrysol.2004.08.056>.
- J.E. Shelby, *Introduction to Glass Science and Technology*, 2nd ed., Royal Society of Chemistry, Cambridge, 2005.
- E.I. Kamitsos, A.P. Patsis, M.A. Karakassides, G.D. Chryssikos, Infrared reflectance spectra of lithium borate glasses, *J. Non-Cryst. Solids* 126 (1–2) (1990) 52–67, [https://doi.org/10.1016/0022-3093\(90\)91023-K](https://doi.org/10.1016/0022-3093(90)91023-K).
- V. Rodriguez, C. Sourisseau, General Maker-fringe ellipsometric analyzes in multilayer nonlinear and linear anisotropic optical media, *J. Opt. Soc. Am. B* 19 (2002) 2650, <https://doi.org/10.1364/JOSAB.19.002650>.
- H. Hosono, Y. Abe, Temperature dependence of infrared absorption spectra of hydroxyl groups in soda germanate glasses, *J. Am. Ceram. Soc.* 72 (1) (1989) 44–48, <https://doi.org/10.1111/j.1151-2916.1989.tb05951.x>.
- Y.D. Yiannopoulos, C.P.E. Varsamis, E.I. Kamitsos, Density of alkali germanate glasses related to structure, *J. Non-Cryst. Solids* 293–295 (2001) 244–249, [https://doi.org/10.1016/S0022-3093\(01\)00677-9](https://doi.org/10.1016/S0022-3093(01)00677-9).
- G. Yang, J. Cao, Y. Qi, X. He, C. Peng, Y. Lu, F. Tang, K. Tang, B. Liu, H. Chen, G. Chen, Y. Gao, D. Chen, Imprinting gradient refractive index micro-structure in GeS₂-Ga₂S₃-KCl glass for broadband diffraction grating, *Opt. Mat.* 101 (2020) 109766, <https://doi.org/10.1016/j.optmat.2020.109766>.

- [43] G.S. Henderson, R.T. Amos, The structure of alkali germanophosphate glasses by Raman spectroscopy, *J. Non-Cryst. Solids* 328 (1–3) (2003) 1–19, [https://doi.org/10.1016/S0022-3093\(03\)00478-2](https://doi.org/10.1016/S0022-3093(03)00478-2).
- [44] R.R. Pereira, F.T. Aquino, A. Ferrier, P. Goldner, R.R. Gonçalves, Nanostructured rare earth doped Nb₂O₅: structural, optical properties and their correlation with photonic applications, *J. Lumin.* 170 (2016) 707–717, <https://doi.org/10.1016/j.jlumin.2015.08.068>.
- [45] G. Monteiro, L.F. Santos, R.M. Almeida, F. D'Acapito, Local structure around Er³⁺ in GeO₂-TeO₂-Nb₂O₅-K₂O glasses and glass-ceramics, *J. Non-Cryst. Solids* 377 (2013) 129–136, <https://doi.org/10.1016/j.jnoncrsol.2012.12.019>.
- [46] M.R. Cicconi, D.K. Dobesh, B. Schroeder, T. Otsuka, T. Hayakawa, D. de Ligny, Alkali-niobate aluminosilicate glasses: structure and properties, *Opt. Mater.* X 18 (2023) 100228, <https://doi.org/10.1016/j.omx.2023.100228>.
- [47] I. Enomoto, Y. Benino, T. Fujiwara, T. Komatsu, Synthesis of nanocrystals in KNb(Ge,Si)O₅ glasses and chemical etching of nanocrystallized glass fibers, *J. Solid State Chem.* 179 (6) (2006) 1821–1829, <https://doi.org/10.1016/j.jssc.2006.03.028>.
- [48] Y. Takahashi, H. Masai, M. Osada, T. Fujiwara, Precursive stage of nanocrystallization in niobium oxide-containing glass, *Appl. Phys. Lett.* 95 (2009) 071909, <https://doi.org/10.1063/1.3211989>.
- [49] P. Pernice, A. Paleari, M. Ferraris, M. Fokine, E. Fanelli, R. Lorenzi, G. Spinolo, A. Aronne, Electric field induced structural modification and second order optical nonlinearity in potassium niobium silicate glass, *J. Non-Cryst. Solids* 355 (52–54) (2009) 2578–2582, <https://doi.org/10.1016/j.jnoncrsol.2009.09.005>.
- [50] M. Micoulaut, L. Cormier, G.S. Henderson, The structure of amorphous, crystalline and liquid GeO₂, *J. Phys. Condens. Matter* 18 (45) (2006) 753–784, <https://doi.org/10.1088/0953-8984/18/45/R01>.
- [51] M. Dussauze, E. Fargin, M. Lahaye, V. Rodriguez, F. Adamietz, Large second-harmonic generation of thermally poled sodium borophosphate glasses, *Opt. Express* 13 (11) (2005) 4064–4069, <https://doi.org/10.1364/OPEX.13.004064>.
- [52] A. Malakho, M. Dussauze, E. Fargin, O. Bidault, V. Rodriguez, F. Adamietz, B. Poumellec, Effect of sodium to barium substitution on the space charge implementation in thermally poled glasses for nonlinear optical applications, *J. Solid State Chem.* 182 (5) (2009) 1156–1163, <https://doi.org/10.1016/j.jssc.2009.02.016>.
- [53] G. Yang, M. Dussauze, V. Rodriguez, F. Adamietz, N. Marquestaut, K.L.N. Deepak, D. Grojo, O. Uteza, P. Delaporte, T. Cardinal, E. Fargin, Large scale micro-structured optical second harmonic generation response imprinted on glass surface by thermal poling, *J. Appl. Phys.* 118 (2015) 043105, <https://doi.org/10.1063/1.4926866>.
- [54] L. Karam, F. Adamietz, V. Rodriguez, F. Bondu, A. Lepicard, T. Cardinal, E. Fargin, K. Richardson, M. Dussauze, The effect of the sodium content on the structure and the optical properties of thermally poled sodium and niobium borophosphate glasses, *J. Appl. Phys.* 128 (2020) 043106, <https://doi.org/10.1063/5.0013383>.
- [55] L. Karam, F. Adamietz, D. Michau, C. Gonçalves, M. Kang, R. Sharma, G. S. Murugan, T. Cardinal, E. Fargin, V. Rodriguez, K.A. Richardson, M. Dussauze, Electrically micro-polarized amorphous sodo-niobate film competing with crystalline lithium niobate second-order optical response, *Adv. Opt. Mater.* 8 (13) (2020) 2000202, <https://doi.org/10.1002/adom.202000202>.
- [56] Y. Qi, Y. Li, Integrated lithium niobate photonics, *Nanophotonics* 9 (6) (2020) 1287–1320, <https://doi.org/10.1515/nanoph-2020-0013>.
- [57] L.M. Marcondes, H. Bradtmüller, S.N.C. dos Santos, L.K. Nolasco, C.R. Mendonça, S.H. Santagneli, G.Y. Poirier, M. Nalin, Structural and luminescence characterization of europium-doped niobium germanate glasses and glass-ceramics: novel insights from ⁹³Nb solid-state NMR spectroscopy, *Ceram. Int.* 48 (14) (2022) 20801–20808, <https://doi.org/10.1016/j.ceramint.2022.04.062>.
- [58] P. Mošner, T. Hostinský, L. Koudelka, Thermal, structural and crystallization study of Na₂O-P₂O₅-Nb₂O₅ glasses, *J. Solid State Chem.* 316 (2022) 123545, <https://doi.org/10.1016/j.jssc.2022.123545>.
- [59] E.I. Kamitsos, Y.D. Yiannopoulos, M.A. Karakassides, G.D. Chryssikos, H. Jain, Raman and infrared structural investigation of xRb₂O-(1-x)GeO₂ glasses, *J. Phys. Chem.* 100 (28) (1996) 11755–11765, <https://doi.org/10.1021/jp960434+>.
- [60] M. Dussauze, O. Bidault, E. Fargin, M. Maglione, V. Rodriguez, Dielectric relaxation induced by a space charge in poled glasses for nonlinear optics, *J. Appl. Phys.* 100 (2006) 034905, <https://doi.org/10.1063/1.2218998>.
- [61] M. Dussauze, T. Cardinal, Nonlinear optical properties of glass, in: J.D. Musgraves, J. Hu, L. Calvez (Eds.), *Springer Handbook of Glass*, Springer International Publishing, 2019, pp. 157–189, <https://doi.org/10.1007/978-3-319-93728-1>. Springer Handbooks.
- [62] P. Dash, M. Yuan, J. Gao, E. Furman, M.T. Lanagan, High electric field conduction in low-alkali boroaluminosilicate glass, *J. Appl. Phys.* 123 (2018) 054102, <https://doi.org/10.1063/1.5004672>.